Electron Transfer in Symmetric Complexes: Displaced Oscillators and $[Fe(CN)_6Pt(NH_3)_4Fe(CN)_6]^{4-}$ Spectra

Margaret H. Hennessy, Ying Wu, Andrew B. Bocarsly,* and Zoltán G. Soos*

Department of Chemistry, Princeton University, Princeton, New Jersey 08544

Received: February 17, 1998; In Final Form: June 1, 1998

Resonance Raman enhancements yield reorganization energies and displacements of individual modes in electron-transfer (ET) spectra when modeled as displaced harmonic oscillators. The same approximations suffice for quantitative simulations of linear absorption, electroabsorption, or Raman excitation profiles (REPs) through the time autocorrelation function for an arbitrary number of displaced modes. Asymmetric absorption profiles in charge-transfer complexes provide both the reorganization energy and solvent broadening. The unusual ET spectra of the trinuclear title compound are associated with nearly localized valences, two excited states, and symmetry-breaking solvent perturbations. Displaced oscillators and diabatic states rationalize broad absorption, structured REPs, and second-derivative electroabsorption with reorganization energies and displacements found in related binuclear complexes. Both a_g and b_u modes are displaced in the centrosymmetric complex and excited-state splitting is related to small polarons. The 1800 cm^{-1} reorganization energy is an order of magnitude smaller than suggested for a single absorption. Raman enhancement data and displaced harmonic oscillators clarify special features of ET or solvents in centrosymmetric complexes.

1. Introduction

Electron transfer (ET) in charge-transfer complexes has been extensively studied[1] in terms of theories developed by Marcus[2] and Hush.[3] The canonical DA complex of a donor and acceptor is inherently polar. Thermal and photochemical ET processes are related by ground (DA) and excited state (D^+A^-) potentials that cross in the limit of no overlap. The central role of potentials leads naturally to electron-vibration coupling and relates ET to charge transport or excitation transfer. Solid-state examples are polarons in ionic crystals, Frenkel excitons in molecular solids, CT excitons in ion-radical salts, and solitons or other self-localized states in conjugated polymers. The Holstein model,[4] a chain with linear coupling of a molecular vibration to an electronic excitation, is the basis for transport theories. Painelli and Girlando[5] discuss the widely different conventions used in various fields.

The shared features of analytical models are a few electronic states, identical harmonic potentials in the ground and excited-state, and linear coupling of electronic and vibrational degrees of freedom. We refer to these approximations collectively as displaced oscillators. The slope of the excited-state potential for a vertical excitation is the linear coupling that defines the curve. Displaced oscillators entail severe approximations that limit molecular applications: anharmonicity, normal mode interactions, quadratic coupling, and additional electronic states are certainly important. Displaced oscillators are nevertheless a robust first approximation for comparing ET or transport in systems that are too complex for complete treatment. They have sharp spectroscopic consequences discussed below. As shown by Hupp[6] and Myers,[7] analysis of Raman enhancements leads directly to geometrical changes accompanying ET. They follow the time-domain formulation of Tannor and Heller,[8] whose coherent state consists of displaced harmonic oscillators.

TABLE 1: Dimensionless Displacements of a_g Modes of $[Fe(CN)_6Pt(NH_3)_4Fe(CN)_6]^{4-}$ Based on Raman Frequencies (cm^{-1}), Relative Enhancements, and Assignments in Reference 9

$\omega(cm^{-1})$	enhancement[a]	assignment	displacement, g
2125	0.80	ν(CN) bridge	0.096
2107	0.20	ν(CN) radial[b]	0.049
624	2.26	ν(Fe−CN) axial	0.54
586	1.00	ν(Fe−CN) radial	0.38
566	2.03	ν(Fe−CN) bridge	0.57
506	0.51	ν(Pt−NH_3)	0.32
472	0.58	δ(Fe−CN)	0.36
420	0.72	δ(Fe−CN)	0.45
366	1.43	ν(Pt−NC) bridge	0.74
299	0.69	δ(H_3N−Pt−NH_3)	0.63

[a] Relative to the 586 cm^{-1} mode. [b] Table 3.1, ref 11.

In this paper, we first extend ET analysis in terms of displaced harmonic oscillators to include solvent broadening. The absorption and Raman excitation profiles (REPs) follow quantitatively and yield more accurate displacements without additional approximations. We then model ET in the centrosymmetric complex $[Fe(CN)_6Pt(NH_3)_4Fe(CN)_6]^{4-}$, and we apply displaced oscillators to REPs and electroabsorption. The complex's many coupled modes illustrate the predictive and organizational capabilities of simulations using displaced oscillators. Indeed, their limitations can only be identified from detailed comparisons.

Resonance Raman spectra provide input frequencies and enhancements of coupled modes, which lead[6] to displacements for assumed harmonic potentials with equal ground and excited-state frequencies. Table 1 contains such data[9] for the centrosymmetric complex. Depolarization ratios were used to identify a_g modes whose assignments follow a related binuclear complex. Relative enhancements are proportional to the displacement or the linear coupling constant. The indicated displacements based on our analysis are considerably smaller

* Corresponding author.

10.1021/jp981181i CCC: $15.00
Published on Web 09/22/1998

than reported[9] using the 8000 cm^{-1} width of the absorption. Displaced oscillators can readily be applied to any complex for which there is Raman enhancement data, and they bring out special features of multiple ET.

The ground state of $[Fe(CN)_6Pt(NH_3)_4Fe(CN)_6]^{4-}$ has metals with formal oxidation **2/4/2**. ET is consistent[10,11] with localized valences and oxidation **3/3/2** or **2/3/3**. Photoinduced ET from Fe(II) to Pt(IV) triggers a second, thermal ET leading to Pt(II) and weak axial bonds in the **3/2/3** complex. Crystal data[12] shows D_{4h} complexes with staggered ligands about the FeC-NPtNCFe (*z*) axis. A direct ET pathway is provided by the overlap of filled Fe(d*xy*) orbitals at either end with the empty Pt(dx^2-y^2) orbital. The complex resembles a head-to-head DA pair (DAAD) in which Pt(IV) can accept two electrons. Localized valences break inversion symmetry and suggest coupling to b_u as well as a_g vibrations. Centrosymmetric complexes have special features that extend to REPs, absorption and electroabsorption. In addition to broadening the spectrum, the solvent can also lift the degeneracy of **3/3/2** and **2/3/3**. These special features motivate our study and show the need for quantitative analysis.

The paper is organized as follows. We relate the vibrational autocorrelation function to Raman data in section 2 and obtain general results for linear absorption and REPs of DA complexes. The **2/4/2** absorption spectrum is modeled in section 3 using Franck−Condon factors for diabatic states. Linear combinations of **3/3/2** and **2/3/3** lead naturally to transitions in two potential wells, thereby increasing the width for the same electron-vibration coupling. We simulate the unusual REPs and electroabsorption of **2/4/2** in section 4 and estimate its reorganization energy, solvent broadening, and excited-state splitting. Quantitative application of displaced oscillators reduces the displacements and revises the interpretation of the first ET in **2/4/2.** We conclude in section 5 with extensions of the model and open questions.

2. Absorption and REP of Displaced Oscillators

We consider ET to a state whose *M* vibrational modes have dimensionless displacements $\mathbf{g} = (g_1,g_2,...,g_M)$ from the ground state. The frequencies $\omega = (\omega_1,\omega_2,...\omega_M)$ are the same as in the ground state by hypothesis. The vibrational state $\mathbf{p} = (p_1,p_2,...p_M)$ has p_j quanta $\hbar\omega_j$ and frequency $\omega\cdot\mathbf{p}$ relative to 0-0. The inner-sphere reorganization energy λ_i for a vertical transition is

$$\lambda_i = \sum_{j=1}^{M} \hbar\omega_j g_j^2 \tag{1}$$

The sum is over $\Delta_j^2/2$ in spectroscopic studies using linear coupling constants $\Delta = g\sqrt{2}$. Reorganization involves all displaced modes and applies equally to allowed and forbidden transitions. The absorption maximum is around λ_i.

The Franck−Condon (FC) overlaps M(**p**) with the ground vibrational state $|0\rangle$ are

$$|M(\vec{p})|^2 = \prod_{j=1}^{M} F_{0p_j}(g_j)^2 = e^{-\vec{g}\cdot\vec{g}} \prod_{j=1}^{M} g_j^{2p_j}/p! \tag{2}$$

The relative intensity $|M(\mathbf{p})|^2$ at $\omega_{00} + \omega\cdot\mathbf{p}$ is fully specified by **g**. The sum over (2) is normalized and partitions an electronic μ_e^2 among vibrational states. We set $\mu_e = 1$ and introduce normalized Lorentzians with equal width, Γ, for each **p** to obtain

$$I(x) = \mathrm{Im}\sum_{\vec{p}} \frac{|M(\vec{p})|^2}{\pi(x - \omega\cdot\vec{p} - i\Gamma)} = \sum_{\vec{p}} \frac{|M(\vec{p})|^2\Gamma/\pi}{(\vec{\omega}\cdot\vec{p} - x)^2 + \Gamma^2} \tag{3}$$

where $x = \omega - \omega_{00}$ is measured from the 0-0 transition. The $\Gamma \to 0$ limit of (3) gives δ-function absorptions at $x = \omega\cdot\mathbf{p}$. The sum has r^M terms when *r* vibrations are kept for each mode, including all overtones and combinations. Direct simulation of *I*(*x*) is consequently laborious even in the Condon approximation for displaced oscillators.

Tannor and Heller[8] showed that *I*(*x*) is conveniently evaluated in the time domain. This is a special case of linear response theory. We use finite Γ instead of δ-functions to bring out additional similarities to Raman scattering. The denominator of (3) is converted to a time integral and the sum over virtual states **p** is carried out using the propagator

$$I(x) = -\mathrm{Re}\int_0^\infty \mathrm{d}t\pi^{-1}\langle\phi_0|\exp(it\sum_j \omega_j b_j^+ b_j)|\phi_0\rangle\exp(-ixt - \Gamma t) \tag{4}$$

The boson operators b_j^+ (b_j) create (annihilate) a quantum $\hbar\omega_j$. The matrix element in (4) is the time autocorrelation function. Zero-point contributions cancel for equal ground and excited-state frequencies and $|0\rangle$ usually suffices for intramolecular modes. Its projection on the excited-state surface is

$$|\phi_0\rangle = [\exp(-\vec{g}\cdot\vec{g}/2 + \sum_j g_j b_j^+)]|0\rangle \tag{5}$$

Taylor expansion of the exponential generates all **p**. Since $b^+(t) = b^+\exp(i\omega t)$ for harmonic oscillators, the autocorrelation function is

$$\langle\phi_0|\phi_0(t)\rangle = \exp(\sum_j g_j^2(e^{i\omega_j t} - 1)) \tag{6}$$

Second quantization yields particularly compact and transparent results for displaced harmonic oscillators in the ground state. The generalization of (5) and (6) to excited oscillators for $kT > \hbar\omega_j$ is straightforward. The autocorrelation function is completely specified by the frequencies ω_j and displacements g_j, which follow within a scale factor from resonance enhancements.

At small t, the reorganization energy (1) is the linear coefficient of t in the exponent in (6), while that of $-t^2/2$ is the sum over $g_j^2\omega_j^2$. These terms are kept in steepest descent, when substitution into (4) gives a Gaussian centered at $x = \lambda_i$ with width related to $g_j^2\omega_j^2$. This limit holds when large *M*, **g**, or Γ cuts off the time integral and is a useful estimate when the excited-state frequencies or displacements are not known. The approximation is superfluous for displaced oscillators, as assumed to obtain relative g_j from resonance enhancements, since the time integral for *I*(*x*) is readily evaluated using (6). In addition, we represent solvent shifts by a normalized Gaussian distribution about ω_{00} with variance σ_s^2. $I(x,\sigma_s)$ is simply (4) with an extra factor of $\exp(-\sigma_s^2t^2/2)$ in the integrand. Displacements based on *I*(*x*) with $\sigma_s = 0$ are upper bounds and accurate absorption profiles or solvent contributions require no additional assumptions.

Doorn et al.[13] studied ET in $[Fe(CN)_6Os(NH_3)_5]^{1-}$ and report $\lambda_i = 2660$ cm^{-1} using a Gaussian approximation for the width of *I*(*x*). The complex's 9 displaced modes (their Table 2) closely match the frequencies in Table 1 and were used[9] to assign the vibrations. The published Δ_j and $\Gamma = 50$ cm^{-1} lead to the asymmetric *I*(*x*) profile in Figure 1a with partly resolved

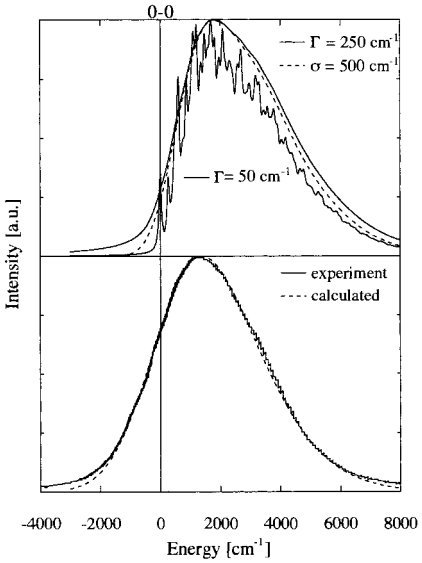

Figure 1. Absorption spectrum of $[Fe(CN)_6Os(NH_3)_5]^{1-}$ relative to 0-0, normalized to equal peak heights. (a) Simulation using (4) and (6) for the 9 displaced modes from Table 2, ref 13, with $\Gamma = 50$ cm^{-1}, 250 cm^{-1}, and solvent broadening $\sigma_s = 500$ cm^{-1}. (b) Experiment from Figure 7, ref 13, and simulation with reoganization energy $\lambda_i = 1800$ cm^{-1}, $\sigma_s = 1250$ cm^{-1}, and $\Gamma = 5$ cm^{-1}, for displacements 25% smaller than in (a).

vibronics; the peak is ~1800 cm^{-1} above 0-0 for these parameters, some 40% below 2660 cm^{-1}. Increasing Γ washes out the vibronic structure, adds intensity below 0-0 and shifts the peak to higher energy; $\Gamma \sim 250$ cm^{-1} or larger appreciably increases the width in Figure 1a. Essentially the same broadening is achieved with $\sigma_s = 500$ cm^{-1}. The curves in Figure 1b are the linear absorption of $[Fe(CN)_6Os(NH_3)_5]^{1-}$ (Figure 7 of ref 13) and a fit based on $\lambda_i = 1800$ cm^{-1}, $\sigma_s = 1250$ cm^{-1}, and negligible Γ (5 cm^{-1}). The fit perceptively improves for smaller λ_i and significant σ_s, although these values are not unique. The width and asymmetry of $I(x)$ are a balance between reorganization and solvent contributions, and this suffices for extracting both λ_i and σ_s.

Kulinowski et al.[14] analyzed the absorption, emission, and reorganization energy of the DA $\rightarrow$ D^+A^- transition in the CT complex hexamethylbenzene/tetracyanoethylene, which has 11 enhanced Raman modes and a broad, symmetric $I(x)$. The decomposition into λ_i and σ_s then requires the extra effort of absolute Raman intensities. The complex also has intermolecular modes[7] whose frequencies are too low to appear in the Raman spectrum and are consequently lumped with the solvent. An asymmetric $I(x)$ simplifies the separation of λ_i for resolved Raman modes from unresolved solvent or low-frequency contributions.

Resonance Raman scattering[8] is closely related to (3) when a single electronic state dominates. We consider 0-1 excitation of mode ω_j at laser frequency $\omega_L = x_L + \omega_{00}$,

$$\alpha_{10}(\omega_j,x_L) = C\sum_{\vec{p}} \frac{|M(\vec{p})|^2 F_{1p_j}(g_j)/F_{0p_j}(g_j)}{x_L - \vec{\omega}\cdot\vec{p} - i\Gamma} \qquad (7)$$

The constant C is independent of **p** and is omitted below, as is the nonresonant part and scattering by other electronic states. Resonance enhancements are proportional to $|\alpha(\omega_j,x_L)|^2$. The FC factors in (7) involving g_j are (dropping the subscript for simplicity)

$$F_{0p}(g)F_{1p}(g) = e^{-g^2}g^{2p-1}(g^2 - p)/q! = -dF_{0p}(g)^2/2dg \qquad (8)$$

Resonant scattering from $|0\rangle$ involves partial derivatives,

$$\alpha_{10}(\omega_j,x_L) = \frac{\partial}{2\partial g_j}\sum_{\vec{p}} \frac{|M(\vec{p})|^2}{x_L - \vec{\omega}\cdot\vec{p} - i\Gamma} \qquad (9)$$

The sum is again the integral (4) over the autocorrelation function (6). The partial leads to

$$\alpha_{10}(\omega_j,x_L) = -2ig_j\int_0^\infty dt(1 - e^{-i\omega_j t})\langle\phi_0|\phi_0(t)\rangle\exp(-\Gamma t - ix_L t) \qquad (10)$$

The real and imaginary parts of (10) give the exact dependence on x_L. We evaluate $|\alpha(\omega_j,x_L)|^2$ as a double integral over time for each displaced oscillator and convolve with a normalized Gaussian whose variance is σ_s^2. The first factor in (10) goes as $\omega_j t$ at the short times of interest for appreciable λ_i and Γ. REPs then scale as $g_j^2\omega_j^2$, the approximation used[6] for the relative displacements. In principle, the complete expression (10) yields more accurate enhancements at x_L.

Since $I(x)$ is normalized, its shape depends on Γ and σ_s but the integrated area is fixed; the value of Γ is then irrelevant when $\Gamma \ll \sigma_s$. The convolution of $|\alpha(\omega_j,x_L)|^2$ with a normalized Gaussian for the solvent also preserves the integrated area as a function of x_L. The total scattering from one or two Lorentzians can readily be shown to increase as Γ^{-1} with decreasing Γ, but only the relative scattering is used for the displacements **g**. Thus convolved $|\alpha(\omega_j,x_L)|^2$ profiles may depend on Γ even when $\Gamma \ll \sigma_s$ due to interference between vibronics.

3. ET in a Symmetric Complex with Localized Valences

Two electronic states, DA and D^+A^-, are traditionally used for CT complexes. Three are needed for the title compound: the **2/4/2** ground state and excited states **3/3/2** and **2/3/3** that we call $|L\rangle$ and $|R\rangle$, respectively. Their minima are shown schematically in Figure 2 for degenerate a_g, b_u modes with displacement g from the ground state at the origin. The final state **3/2/3** enters in the second, thermal ET and is not used below. In the ground-state geometry, we have splitting 2J between even and odd linear combinations

$$|2A\rangle,|1B\rangle = (|L\rangle \pm |R\rangle)/\sqrt{2} \qquad (11)$$

The usual approximation of neglecting overlap is particularly good here because $|L\rangle$ and $|R\rangle$ have different occupancy in Fe orbitals separated by a CNPtNC bridge. In addition to $\langle L|H|R\rangle$, which corresponds to excitation transfer, there are second-order contributions to J due to configuration interaction. Mixing of $|2A\rangle$ with the ground state places it above $|1B\rangle$, while the head-to-head orientation of transition moments suggests that $|1B\rangle$ is higher. We exclude strict degeneracy on physical grounds for the approximate states (11). We start with localized valences and finite J for an isolated complex and then generalize to symmetry breaking by the solvent.

The $Fe(CN)_6^{4-}$ modes in Table 1 are closely related to those[13] of $Fe(CN)_6Os(NH_3)_5^{1-}$; the second metal center is a small perturbation. It follows that a_g modes of **2/4/2** have b_u partners with almost the same frequency, displacement, and out-of-phase $Fe(CN)_6^{4-}$ motions. Table 1 leads to M = 18 displaced modes, since in-plane $Pt(NH_3)_4^{4+}$ modes have no b_u partners. We choose modes (ω_j, g_j), drop the subscript j, and define operators b_1^+,b_1 for $|L\rangle$ and b_2^+,b_2 for $|R\rangle$. The transformation

$$b^+_{s,a} = (b^+_1 + b^+_2)/\sqrt{2} \quad (12)$$

resolves them into symmetric (a_g) vibrations along *y* in Figure 2 and antisymmetric (b_u) vibrations along *x*, with displacements (−g,g) and (g,g). The two modes contribute $2\hbar\omega_j g_j^2$ to (1) in either the localized or delocalized representation.

Displaced harmonic potentials are sketched in Figure 3 for an a_g, b_u pair. Vibrations in the $x = 0$ plane resemble standard ET curves for an excited state with minimum at $y = g$. Antisymmetric vibrations in the $y = 0$ plane have minima at $x = \pm g$ for $|R\rangle$ and $|L\rangle$; the intersection at x = 0 becomes an avoided crossing, 2*J*, when excitation transfer is included. The harmonic potentials in Figure 3 differ from ET curves for free energy changes, $\lambda = \lambda_i + \lambda_s$, that include solvent. Free energies involve a generalized reaction coordinate, a one-dimensional representation of a collective motion, rather than individual normal modes. The full λ = 14700 cm^{-1} for **2/4/2** is estimated[10b,11] directly from the absorption peak and the thermal barrier for the first ET.

Vertical excitation to $|1B\rangle$ is dipole allowed and gives a superposition of diabatic states. The generalization of (5) for a single a_g, b_u pair is an odd-parity state

$$|X,g\rangle = 2^{-1/2}(|L\rangle\exp(-g^2 + g\sqrt{2}b_1^+) - |R\rangle\exp(-g^2 + g\sqrt{2}b_2^+))|0\rangle \quad (13)$$

where the displacement is $g\sqrt{2}$ in either $|L\rangle$ or $|R\rangle$ and the $g = 0$ limit is $|1B\rangle|0\rangle$. The corresponding even-parity function $|Y,g\rangle$ is the even linear combination of (13) and reduces to $|2A\rangle|0\rangle$ at g = 0. We use (11) and (12) to resolve the local excitations into symmetric and antisymmetric parts, expand the operators and collect terms to obtain

$$|X,g\rangle = e^{-g^2+gb_s^+}(|1B\rangle\cosh(gb_a^+) + |2A\rangle\sinh(gb_a^+))|0\rangle \quad (14)$$

The first term is even vibrationally, restricted to an even numbers of b_u quanta, and is odd electronically. The second term necessarily has an odd number of b_u quanta and consequently appears with an even electronic state. The generalization to *M* modes is to sum over b_s and b_a in (14). The vibronic **p** appears in the first (second) term if the total number of quanta in b_u modes is even (odd).

The linear absorption contains even **p** of $|1B\rangle$ and odd **p** of $|2A\rangle$. The time autocorrelation function (6) for $|1B\rangle$ vibronics becomes

$$\langle\phi_1|\phi_1(t)\rangle = (\exp[-\vec{g}\cdot\vec{g} + \sum_s g_s^2 e^{i\omega_s t}])\cosh(\sum_a g_a^2 e^{i\omega_a t}) \quad (15)$$

for the ground vibrational state. We insert in (4) and integrate to obtain $I_1(x)$. The corresponding expression for odd vibronics of $|2A\rangle$ is

$$\langle\phi_2|\phi_2(t)\rangle = (\exp[-\vec{g}\cdot\vec{g} + \sum_s g_s^2 e^{i\omega_s t}])\sinh(\sum_a g_a^2 e^{i\omega_a t}) \quad (16)$$

and there in an additional factor of $\exp(2iJt/\hbar)$ in (4) for the $I_2(x)$. The full spectrum, $I_1(x)+I_2(x)$, is illustrated in Figure 4 for $2J \sim \lambda_i$ and may be resolved for $J > \lambda_i$.

The linear absorption[10] of **2/4/2** in Figure 4 has a broad peak whose ∼8000 cm^{-1} width is almost twice that of the FeOs complex in Figure 1. Comparable λ_i is expected on physical grounds for closely related vibrations. The solid line in Figure 4 is a fit based on Table 1 and λ_i = 1800 cm^{-1}, σ_s = 1500 cm^{-1}, Γ = 5 cm^{-1}, J = −1800 cm^{-1}. Negative *J* places $|1B\rangle$ at higher energy, as expected for head-to-head transition dipoles, and 0-0 is the sharp central spike in the high-resolution simulation. The $|2A,\mathbf{p}\rangle$ vibronics of the lower state contain at least one b_u quantum. Quantitative fits require larger σ_s ∼1900 cm^{-1}, smaller J = -1600 cm^{-1}, and correcting the high energy data for a nearby metal-to-ligand CT.[10] The dashed line in Figure 4 is a simulation with the same parameters except for J = −1900 cm^{-1} and 10% changes of b_u displacements as described in the Discussion. The simulated $I(x)$ are quite similar and more structured than experiment; they lead to different REP profiles in section 4.

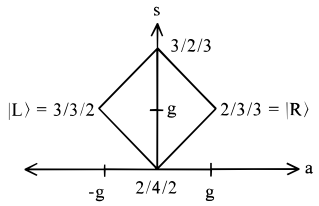

Figure 2. Displacements $g\sqrt{2}$ of a local mode of **3/3/2** or **2/3/3** relative to the ground state, **2/4/2**, and their resolution into symmetric (a_g) and antisymmetric (b_u) modes of the complex; a second ET leads to **3/2/3**.

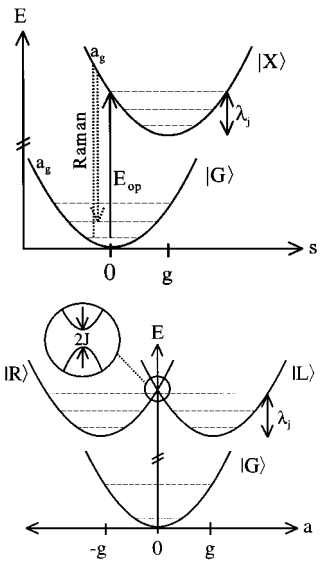

Figure 3. (a) Schematic potential of the ground and excited state for a displaced a_g mode; the reorganization energy, linear absorption, and resonance Raman scattering are indicated. (b) Diabatic potentials for a displaced b_u mode, with excited-state crossing for $J = 0$.

The displacements in Table 1 are smaller by a factor of 5.75 from the Δ in Table 1 of ref 9. A $\sqrt{2}$ reduction is simply due to the definition $g = \Delta/\sqrt{2}$ and another factor of 1.3 is due to b_u contributions to $I(x)$, instead of attributing the full width to a_g modes. The remaining factor of 3.1 reflects the assumption of a single electronic absorption. Broader lines exacerbate the error of using a Gaussian width rather than the autocorrelation function (6). The estimated[9] reorganization energy of 16,500 cm^{-1} from the width does not reproduce $I(x)$ in Figure 4, but in fact places 0-0 so far below the measured $\lambda_i + \lambda_s$ that the excited-state minimum falls *below* the ground state. Substantially smaller displacements are clearly required even for J = 0, when the entire width is assigned to λ_i and σ_s. We take $J \neq 0$ partly because localized valences suggest nearby $|1B\rangle$, $|2A\rangle$ states in centrosymmetric complexes and partly to understand REP and electroabsorption spectra.

Solvent broadening σ_s represents the modulation of ω_{00} as discussed in section 2. In the three-level **2/4/2** system, the solvent also lifts the degeneracy of **3/3/2** and **2/3/3** whenever

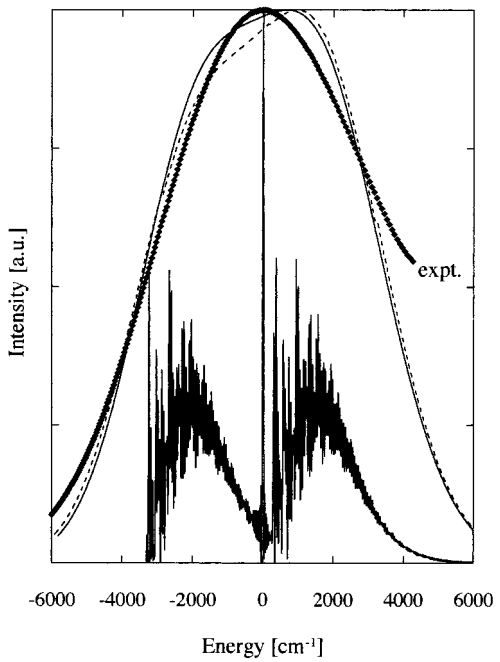

Figure 4. Linear absorption of $[Fe(CN)_6Pt(NH_3)_4Fe(CN)_6]^{4-}$ relative to 0-0 of $|1B\rangle$: experiment from Figure 1, ref 10a, simulations using (4), (15), and (16) for displacements in Table 1. The resolved spectrum has $J = -1800$ cm^{-1} and becomes the solid line for solvent broadening $\sigma_s = 1500$ cm^{-1}; the dashed line has the same σ_s, $J = -1900$ cm^{-1}, and 10% changes in displacements as discussed in the text.

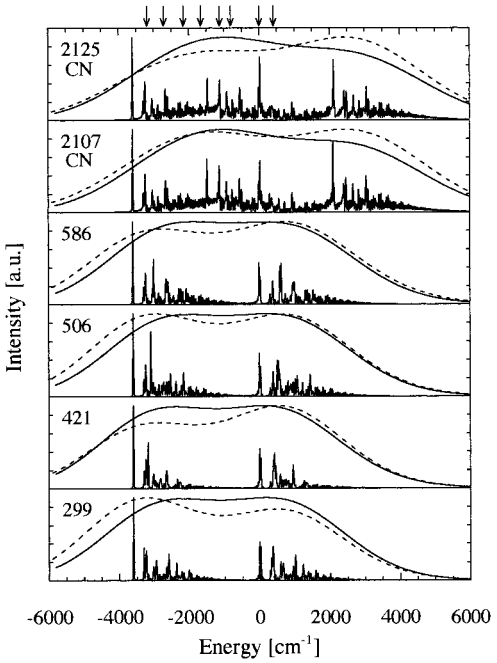

Figure 5. Simulated Raman enhacement profiles, in arbitrary units, for six of the a_g modes in Table 1 and the parameters in Figure 4 for the resolved, solid and dashed lines. The arrows (top) indicate the laser frequencies used in ref 9 to measure enhancements.

the surrounding ions preferentially stabilize $|R\rangle$ or $|L\rangle$. We define 2Δ as the solvent-induced splitting and choose $|1B\rangle$ to be the upper state at $|J|$ when $\Delta = 0$. The mixing of $|R\rangle$ and $|L\rangle$ is a standard problem. The electronic energies are $\pm\epsilon$, with $\epsilon^2 = (\Delta^2 + J^2)$; the eigenfunctions depend on J/Δ; $|R\rangle$ and $|L\rangle$ have identical vibronics for any admixture. The dipole operator connects the ground state to $|X,g\rangle$, as indicated in (13), and the resolution of local modes into a_g, b_u pairs goes through as before. Only the electronic states are different for $\Delta > 0$. Following the previous development, we obtain

$$I(x,\Delta) = \mathrm{Im}\sum_{\vec{p}}\frac{|M(\vec{p})|^2}{2\pi}\left\{\frac{1-(-1)^pJ/\epsilon}{\vec{\omega}\cdot\vec{p}-\epsilon-x-i\Gamma}+\frac{1+(-1)^pJ/\epsilon}{\vec{\omega}\cdot\vec{p}+\epsilon-x-i\Gamma}\right\} \quad (17)$$

The sum is over both a_g and b_u modes. We regain the $\Delta = 0$ results when $|1B\rangle$ is the upper state, with only even **p**, while only odd **p** occurs in the lower state. The $\Delta \gg J$ limit leads as expected to equal intensity for $|R\rangle$ and $|L\rangle$ vibronics of the uncoupled system. The integrated absorption does not depend on Δ.

4. Resonance Excitation Profiles and Electroabsorption

We use $\alpha(\omega_s,x_L)$ in (10) to calculate REPs of a_g modes. The contribution to $\alpha(\omega_s,x_L)$ from the $|1B\rangle$ surface contains the autocorrelation function (15). The $|2A\rangle$ contribution is based on (16) and has a factor $\exp(2iJt/\hbar)$ in (10). The amplitude is found before introducing σ_s, since the solvent is static on the Raman time scale; $\Gamma = 5$ cm^{-1} gives a convenient upper limit of integration in (10) without appreciable broadening.

Representative $|\alpha(\omega_s,x_L)|^2$ curves for a_g modes in Table 1 are the resolved REPs in Figure 5, with $J = -1800$ cm^{-1} and other $I(x)$ parameters in Figure 4. Resolved REPs become the solid curves on convolving with a Gaussian with $\sigma_s = 1500$ cm^{-1}. The dashed curves have $J = -1900$ cm^{-1}, $\sigma_s = 1500$ cm^{-1}, and 10% changes of b_u displacements. The two simulations lead to different profiles and vary from mode to mode. The solvent reduces, but does not suppress, the electronic splitting. We find similar REPs for $\Delta > 0$ and comparable splitting, $2\epsilon = 3600$ cm^{-1}. The calculated REPs have broad maxima $\sim$3000 cm^{-1} below the absorption peak for low-frequency modes and $\sim$1000 cm^{-1} below the peak for CN stretches.

The experimental REPs in Figure 3 of ref 9 are based on the eight laser frequencies ω_L, marked as arrows at the top of Figure 5. The two CN modes are similar and differ from low-frequency modes that resemble the calculated REPs in having a broad maximum $\sim$3000 cm^{-1} below the absorption peak and a (deeper) minimum at the peak. The reported[9] CN features are much sharper, with a minimum at the peak and a maximum $\sim$500 cm^{-1} lower in energy. The observed REP minima at the peak are emphasized[9] and several qualitative explanations are sketched in terms of additional electronic states. Localized valences and displaced harmonic oscillators account for REP minima directly in terms of excited-state splitting and properly locate the maxima of the low-frequency modes in Table 1. The CN profiles are not reproduced and such sharp features seem incompatible with our parameters. We defer possible improvements of the model to the Discussion and note that REP spectra indicate that J or ϵ is at least as large as λ_i.

We turn next to electroabsorption (EA) and the implications of the identical vibronic structure of $|X,\mathbf{g}\rangle$ and $|Y,\mathbf{g}\rangle$, the many-mode generalizations of (13). A static electric field F mixes states of opposite parity. To order F^2 in the differential absorption, we have shifts and bleaching of dipole-allowed states and induced absorption at two-photon states. A field F along z splits the degeneracy of $|L\rangle$ and $|R\rangle$ in (11) by $2\mu_L F$, where μ_L is the dipole moment of **3/3/2** in the ground-state geometry. The electronic dipole operator μ_z gives $\mu_z|1B\rangle = \mu_L|2A\rangle$, and vice versa, as verified from (11) and (13). We neglect any field

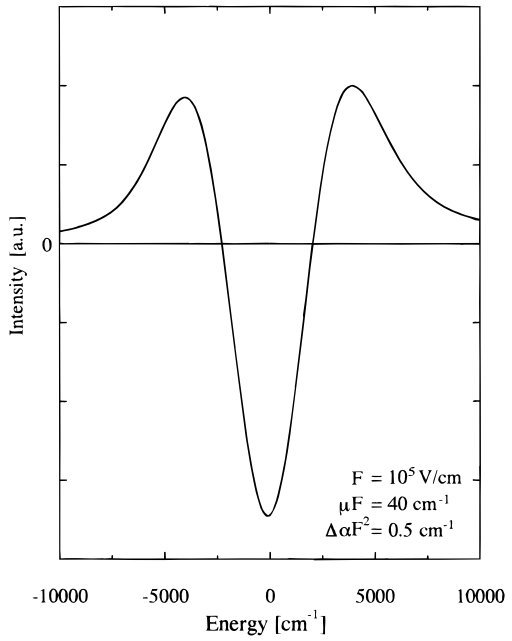

Figure 6. Simulated electroabsorption spectrum of **2/4/2**, in arbitrary units, with the origin at 0-0 of $|1B\rangle$ and absorption given by the solid line in Figure 4. The dipole μ_L is 20 D and the polarizability difference is 100 Å^3.

dependence for the vibrations. Displaced oscillators simplify the analysis enormously. The mixing is diagonal in **p** for states with identical vibronic structure; each **p** of $|1B\rangle$ mixes exclusively with the same **p** of $|2A\rangle$.

Dipole-allowed absorptions to *even* **p** of $|1B\rangle$ lead to $I_1(x)$, while *odd* **p** of $|2A\rangle$ give $I_2(x)$. Since EA is a linear process, we can treat contributions separately and start with *even* **p** and $I_1(x)$. Mixing of $|1B,\mathbf{p}\rangle$ and $|2A,\mathbf{p}\rangle$ produces a Stark shift and transfers intensity to the two-photon state.[15] The EA spectrum is the differential absorption,

$$EA_1(x,\vec{p}) = \cos^2\varphi\, I_1(x(\vec{p}) + \hbar\delta\omega_1) + \sin^2\varphi\, I_1(x(\vec{p}) - 2J) - I_1(x(\vec{p})) \quad (18)$$

Here $x(\mathbf{p}) = x - \omega\cdot\mathbf{p}$ is the absorption (3) relative to ω_{00}, $\delta\omega_1$ is the Stark shift, and φ is the field-induced mixing,

$$\hbar\delta\omega_1 = -(J^2 + \mu_L^2F^2)^{1/2} + |J| + (\alpha_{1B} - \alpha_G)F^2/2$$
$$\tan 2\varphi = \mu_L F/|J| \quad (19)$$

Since $\sin^2\varphi$ goes as F^2, we can neglect the Stark shift in the second term of (18). The polarizability difference $\alpha_{1B} - \alpha_G$ in (19) describes all other electronic states. Since neither $\delta\omega_1$ nor φ depends on **p**, we sum (18) over even **p** to obtain[15]

$$EA_1(x) = \cos^2\varphi\, I_1(x + \delta\omega_1) + \sin^2\varphi\, I_1(x - 2J) - I_1(x) \quad (20)$$

This simple general result holds when F mixes electronic states with identical vibronics **p**, as required for (18), and the mixing does not depend on **p**.

EA spectra are usually analyzed in terms of the linear absorption (3) and its frequency derivatives.[16,17] Stark shifts for $F \sim 10^5$ V/ cm are ~0.5 cm^{-1} for a 100 Å^3 polarizability change and ~40 cm^{-1} when μ_L is an electron transfer over 5 Å (the Fe−Pt separation is[12] 4.99 Å). When $\delta\omega_1$ is small compared to the observed width, we rewrite (20) as

$$EA_1(x) = \delta\omega_1\frac{\partial I_1(x)}{\partial x} + \sin^2\varphi\,[I_1(x - 2J) - I_1(x)] \quad (21)$$

A resolved peak at $2J$ clearly requires a splitting larger than the experimental line width. When the width exceeds $2J$, the second term of (21) is a derivative and we have, to order F^2,

$$EA_1(x) = 1/2(\alpha_{1B} - \alpha_G)F^2\frac{\partial I_1(x)}{\partial x} + \frac{\mu_L^2F^2}{2|J|}\left\{\frac{\partial I_1(x + |J|)}{\partial x} - \frac{\partial I_1(x)}{\partial x}\right\} \quad (22)$$

on using (19) to simplify $\sin^2\varphi$. The second term is $(\mu_L F)^2/2$ times the second derivative, $\partial^2 I_1(x)/\partial x^2$, for small J.

The same analysis holds for *odd* **p** and $I_2(x)$. The field now mixes dipole-allowed states $|2A,\mathbf{p}\rangle$ with two-photon states $|1B,\mathbf{p}\rangle$ at higher energy. We have

$$EA_2(x) = \cos^2\varphi\, I_2(x - 2J + \delta\omega_2) + \sin^2\varphi\, I_2(x) - I_2(x - 2J) \quad (23)$$

for induced absorption at x and bleaching at $x + 2|J|$. The Stark shift $\delta\omega_2$ is given by (19) with the opposite sign for the J terms, since the shift is now to the red. The polarizability change due to other states is approximately the same and yields a first derivative,

$$EA_2(x) = 1/2(\alpha_{2A} - \alpha_G)F^2\frac{\partial I_2(x)}{\partial x} + \frac{\mu_L^2F^2}{2|J|}\left\{\frac{\partial I_2(x + 2|J|)}{\partial x} - \frac{\partial I_2(x + |J|)}{\partial x}\right\} \quad (24)$$

The second term again reduces to $(\mu_L F)^2/2$ times $\partial^2 I_2(x)/\partial x^2$ when J is small compared to the absorption width.

The EA spectrum is $EA_1(x) + EA_2(x)$; the $I'(x)$ and $I''(x)$ contributions both add. $I'(x)$ describes polarizability changes for any complex, while $I''(x)$ gives the mixing of $|1B,\mathbf{p}\rangle$ and $|2A,\mathbf{p}\rangle$ in a centrosymmetric complex. EA simulations for arbitrary J are conveniently based on (20) and (23), which require no assumptions about line widths. The calculated spectrum in Figure 6 is based on the linear absorption in Figure 4, with $\sigma_s = 1500$ cm^{-1}, $\Gamma = 5$ cm^{-1}, $\mu_L = 20$ D, and a typical polarizability change[18] of 100 Å^3 between the ground and excited state. The EA spectrum in Figure 6 resembles $I''(x)$, with a minimum close to the origin marking the 0-0 spike in Figure 4. The large high-energy feature is due to the simulated $I(x)$ in Figure 4, whose greatest curvature is above the peak, while the experimental absorption's greatest curvature is below the peak. Figure 4.1 of ref 11 has a preliminary EA spectrum of **2/4/2** in frozen solution at 80 K. It shows a dominant $I''(x)$ shape consistent with an ET of 5 Å ($\mu_L \sim 20$ D using Liptay analysis[16a]). The absorption is over 2000 cm^{-1} narrower at 80 K and its peak matches the EA minimum.

Small J generates $I''(x)$ by mixing nearby even and odd-parity states in centrosymmetric systems, without averaging over different orientations of the field. Thus (22) or (24) are conceptually different from EA analysis of CT complexes,[16] where an orientational average produces an $I''(x)$ term and first-order Stark shifts are not considered. We comment below on the extent to which **2/4/2** can be approximated by two noninteracting CT complexes, as assumed implicitly in previous work.

5. Discussion

Reorganization energies of individual modes and bond-length changes follow directly from Raman enhancements when

specific assumptions are made about the excited-state potential.[6] The resulting model of displaced harmonic oscillators is the coherent state of Tannor and Heller.[8] The assumptions needed to extract displacements are sufficient for quantitative simulations of spectra in terms of the autocorrelation function (6) for a DA dimer in the ground state and from (15) and (16) for the diabatic states of **2/4/2**. In either case, the propagation of the vibrational ground state on the excited-state surface follows from the *same* Raman data. We find significant revisions of reorganization energies, especially in the centrosymmetric complex.

The autocorrelation function reduces the absorption spectrum for any number of displaced oscillators to a single time integration, as shown for $[Fe(CN)_6Os(NH_3)_5]^{1-}$ in Figure 1. Because the Franck-Condon profile is asymmetric, with a sharp 0-0 edge, solvent broadening $\sigma_s \sim 1250$ cm^{-1} can readily be extracted in addition to $\lambda_i \sim 1800$ cm^{-1}. The reorganization energy is 40% lower than the 2660 cm^{-1} inferred from the width alone.[13] The dimensionless displacements g_j, and hence all bond-length changes, are reduced by 25%.

The interpretation of $[Fe(CN)_6Pt(NH_3)_4Fe(CN)_6]^{4-}$ spectra changes substantially: $\lambda_i \sim 1800$ cm^{-1} is almost an order of magnitude smaller than the 16500 cm^{-1} estimated[9] from the width. The inferred g_j in Table 1 are 4.1 times smaller. One third is due to having b_u and a_g displacements; the rest comes from the broad, unresolved **2/4/2** absorption in Figure 4. The absence of harmonics in the Raman spectra was puzzling for large displacements, but readily understood for reduced $g_j < 1$. The identification of two excited states follows naturally from displaced oscillators and rationalizes other **2/4/2** spectra, notably the REP minima and maxima of low-frequency modes in Figure 5, while the sharp REPs reported for CN disagree with simulations. The EA spectrum is consistent with two active electronic states. We chose identical $\lambda_i = 1800$ cm^{-1} for ET in closely related complexes, but differences up to 10% could easily occur.

Localized valences and solvent contributions are special features of **2/4/2**. In addition to broadening, the solvent lowers the symmetry as recognized[7] previously for photodissociation of I_3^-. The solvent splitting 2Δ between $|L\rangle$ and $|R\rangle$ is expected to be comparable to σ_s. We first suppose that ions or dipoles generate a static electric field at the complex. Since the z component shifts ET in opposite directions for head-to-head dipoles, we have $\Delta = \sigma_s$ due to long-range interactions for anticorrelated transitions. In the opposite limit of short-range interactions, the transitions are uncorrelated and Δ is $\sigma_s/\sqrt{2}$. Since the complex and solvent have comparable size, the transitions are partially anticorrelated for head-to-head dipoles and $\Delta \sim \sigma_s$. We used $\sigma_s = 1250$ cm^{-1} for the binuclear complex in Figure 1 and a somewhat underestimated $\sigma_s = 1500$ cm^{-1} for **2/4/2** in Figures 4−6. We therefore expect $\Delta > 1200$ cm^{-1} and $J \sim \Delta$ or less based on $I(x)$ and REP simulations with $\epsilon = 1800$ cm^{-1}. Rough estimates demonstrate the solvent's importance and competition between Δ and J.

The solvent gives the outer-sphere reorganization energy λ_s. The classical limit for low-frequency oscillators leads to[19]

$$\sigma_s^2 = 2\lambda_s kT \tag{25}$$

We have $\lambda_s \sim 6000$ cm^{-1} for $\sigma_s = 1500$ cm^{-1} at 300 K and add $\lambda_i + \epsilon \sim 4000$ cm^{-1} for the apparent reorganization energy, since the **2/4/2** peak in Figure 4 has an unresolved splitting. The measured[11] $\lambda = h\nu_{max} - \Delta E$ is 14700 cm^{-1} is slightly larger and corresponds to $\sigma_s \sim 2000$ cm^{-1}. The broadening obtained from simulated spectra is satisfactory and we could almost have taken σ_s as fixed rather than adjustable. Larger $\Delta \sim \sigma_s$ in turn reduces the inferred J and supports the picture of nearly localized valences. The largest contribution to λ comes from the solvent, and (25) is consistent with the strong (>2000 cm^{-1}) narrowing of the absorption at 80 K.[11] The observed width also changes with the hydrogen-bonding ability of the solvent,[10b] indicative of σ_s variations.

Localized valences bring out a useful analogy between **2/4/2** and a hypothetical DAAD system whose DA moeities can be treated according to Liptay.[16a] The usual choice of μ_g for the DA and μ_e for D^+A^- leads to $\mu_L = \mu_e - \mu_g$ for $|L\rangle$. The centrosymmetric **2/4/2** ground state has vanishing dipole moment, as do the states $|1B\rangle$ and $|2A\rangle$ in (11). The dipole moment *change* for excitation to $|L\rangle$ or $|R\rangle$ is $\pm \mu_L$, precisely the same as in a DA complex; thus the coefficient $(\mu_L F)^2$ of the $I''(x)$ term in EA is also the same. Head-to-head geometry ensures an exact correspondence between EA in the $J = 0$ limit and DA complexes in solution. The broad absorption leads to equally broad $I''(x)$ contributions. On the other hand, noninteracting DA complexes do not account for structured REPs. Such comparisons show the limitations of the instructive DAAD limit and the need for finite J.

The solvent and temperature dependencies of **2/4/2** spectra provide wider applications of displaced oscillators. Such studies are in progress. Detailed modeling of dimers with finite hopping J and symmetry breaking Δ are theoretical extensions sketched below. Displaced oscillators can also be used to improve the Raman inputs through the complete expression (10) for $\alpha(\omega_j, x_L)$. The resonance enhancement $|\alpha(\omega_j, x_L)|^2$ necessarily scales as g_j^2 in linear-coupling models. The assumed scaling as ω_j^2, by contrast, is the leading term for $\omega_j t \ll 1$. It then follows that all REPs are identical, since the integrand of (10) is independent of j after factoring out ω_j. The different profiles in Figure 5 indicate that higher-order contributions in ω_j are not negligible. We also find mode-dependent REPs in the simpler FeOs complex for the $I(x)$ parameters in Figure 1b. Just as for linear absorption, quantitative REPs follow directly for displaced harmonic oscillators. Accurate modeling is a prerequisite for identifying failures or inconsistencies of displaced oscillators with equal ground and excited-state frequencies.

The theoretical analysis can also be deepened without additional experimental input. Displaced oscillators are the starting point for polarons or excitons in extended systems.[4] Double-well potentials such as in Figure 3b are closely related to the Holstein model, with a single coupled mode, and were discussed by Fulton and Gouterman[20] for dimers. The diabatic states (13) are the special case for $J = 0$. Finite J implies excitation transfer between $|L\rangle$ and $|R\rangle$ that corresponds to the dimer version of the small polaron. Appropriate vibrational functions for a few b_u modes can be obtained numerically[21] and there are some analytical limits, but not a general solution.

In dimers, a_g vibrations are not coupled and displaced oscillators remain appropriate for finite J. The **2/4/2** fits give the $\hbar\omega g^2$ in Table 1 that account for over half of the reorganization energy. The b_u contribution to λ_i is $\lambda_a \sim 800$ cm^{-1}, or $\sim J/2$ used in the simulations. Merrifield's variational procedure[22] postulates displacements on *both* sites in $|L\rangle$ or $|R\rangle$ as a function of J/λ_a. The upper and lower states, $|1B\rangle$ and $|2A\rangle$ for $J < 0$, have different equilibrium displacements.[23] The total energy in the upper state is reduced by out-of-phase distortions of the two sites along the antisymmetric coordinate in Figure 2. The excited-state displacements and hence λ_a increase compared to $J = 0$. The displacements are in-phase

in the lower state, reduced from λ_a. A sum rule ensures that the total excited-state displacement is conserved for linear coupling to vibrations. The $J = 0$ displacements for a_g modes obtained from Raman data are retained for finite J, while the b_u displacements increase (decrease) with J in the upper (lower) state.[23] The variational calculation is straightforward at $\Delta = 0$, without symmetry breaking by the solvent.

Linear electron-vibration coupling leads to anharmonic potentials along antisymmetric coordinates for finite J. Approximations of various sorts are then needed. As a *heuristic* example, we suppose that g_a for each antisymmetric mode is increased by 10% in (15), decreased by 10% in (16). The resulting dashed lines in Figures 4 and 5 show that, although broad, the spectra are sensitive to modest parameter changes. More rigorously, the b_u displacements depend on $J/\hbar\omega_j$, low-frequency modes change the most, and there are frequency shifts and altered Franck−Condon factors. Detailed analysis is certainly possible and needed for improved simulations of additional spectra. Such developments are extensions that retain the original assumptions about linear coupling and harmonic potentials at $J = 0$.

In summary, we have obtained quantitative consequences of displaced harmonic oscillators for ET spectra and presented a simple general expression for the linear absorption and solvent broadening. Displaced oscillators rationalize the special features of **2/4/2** associated with nearly localized valences, head-to-head transition moments, and solvent contributions, and do so with the reorganization energy of a related CT complex. Within approximations introduced for resonance Raman enhancements, displaced oscillators yield quantitative simulations of linear and electroabsorption, as well as resonance enhancement profiles for diabatic states. A consistent approach to different spectra and to solvent contributions suggests experimental comparisons that are in progress. Theoretical improvements of the model focus on finite J, the excited-state splitting of **2/4/2** that relates ET to polaron models.

Acknowledgment. Z.G.S. thanks K. Lehmann, A. Painelli, and R.H. Young for stimulating discussions about oscillators strengths, diabatic states, and solvent broadening, and A.B.B. thanks D. Watson. We gratefully acknowledge support of this work by the National Science Foundation through Grants DMR-9530116 and CHE-963180.

References and Notes

(1) (a) Barbara, P. F.; Meyer, T. J.; Ratner, M. A. *J. Phys. Chem.* **1996**, *100*, 13148. (b) Ondrechen, M. J. *Int. Rev. Phys. Chem.* **1995**, *14*, 1.

(2) (a) Marcus, R. A. *Annu. Rev. Phys. Chem.* **1964**, *15*, 155. (b) Marcus, R. A. *Rev. Mod. Phys.* **1993**, *65*, 599.

(3) (a) Hush, N. S. *Prog. Inorg. Chem.* **1957**, *8*, 391. (b) Hush, N. S. *Electrochim. Acta* **1968**, *13*, 1005. (b) Reimers, J. R.; Hush, N. S. *J. Phys. Chem.* **1991**, *95*, 9773.

(4) (a) Holstein, T. *Ann. Phys.* **1959**, *8*, 325, 345. (b) Emin, D. *Adv. Phys.* **1973**, *22*, 57.

(5) Painelli, A.; Girlando, A. *J. Chem. Phys.* **1986**, *84*, 5655.

(6) Doorn, S. K., Hupp, J. T. *J. Am. Chem. Soc.* **1989**, *111*, 1142, 4712.

(7) (a) Myers, A. B. *Acc. Chem. Res.* **1997**, *30*, 519; (b) *Chem. Rev.* **1996**, *96*, 911.

(8) Tannor, D. J.; Heller, E. J. *J. Chem. Phys.* **1982**, *77*, 202.

(9) Pfennig, B. W.; Wu, Y.; Kumble, R.; Spiro, T. G.; Bocarsly, A. B. *J. Phys. Chem.* **1996**, *100*, 5745.

(10) (a) Pfennig, B. W.; Bocarsly, A. B. *J. Phys. Chem.* **1992**, *96*, 226. (b) Wu, Y.; Cohran, C.; Bocarsly, A. B. *Inorg. Chim. Acta* **1994**, *226*, 251.

(11) Wu, Y. Ph.D. Thesis, Princeton University, 1996 and references therein.

(12) Zhou, M.; Pfennig, B. W.; Steiger, J.; Van Engen, D.; Bocarsly, A. B. *Inorg. Chem.* **1990**, *29*, 2456.

(13) Doorn, S. K.; Blackburn, R. L.; Johnson, C. S.; Hupp, J. T. *Electrochim. Acta* **1991**, *36*, 1775.

(14) Kulinowski, K.; Gould, I. R.; Myers, A. B. *J. Phys. Chem.* **1995**, *99*, 9017.

(15) Soos, Z. G.; Mukhopadhyay, D.; Hennessy, M. H. *Chem. Phys.* **1996**, *210*, 249.

(16) (a) Liptay, W. In *Modern Quantum Chemistry*; Sinanoglu, O., Ed.; Acedemic: New York, 1965; Vol. III, p 45. (b) Sebastian, L.; Weiser, G.; Bässler, H. *Chem. Phys.* **1981**, *61*, 125.

(17) Aspnes, D. E; Rowe, J. E. *Phys. Rev.* **1972**, *B5*, 4022.

(18) Oh, D. H.; Sano, M.; Boxer, S. G. *J. Am. Chem. Soc.* **1991**, *113*, 6880.

(19) Marcus, R. A. *J. Phys. Chem.* **1989**, *93*, 3078.

(20) Fulton, R. L.; Gouterman, M. *J. Chem. Phys.* **1964**, *41*, 2280.

(21) Pepho, S. B.; Krausz, E. R.; Schatz, P. N. *J. Am. Chem. Soc.* **1978**, *100*, 2996.

(22) Merrifield, R. A. *J. Chem. Phys.* **1964**, *44*, 4450.

(23) Hennessy, M. H.; Soos, Z. G.; Bulovic, V.; Forrest, S. R. In *Electrical, Optical and Magnetic Properties of Organic Solid-State Materials IV*; Reynolds, J. R., Jen, K.-Y., Dalton, L., Rubner, M. F., Chiang, L. Y., Eds.; MRS Symposium Series 488; Materials Research Society: Warrendale, PA, 1998; p 101.